



Electrochemical properties of the polyethylene oxide–Li(CF₃SO₂)₂N and ionic liquid composite electrolyte

H. Wang, N. Imanishi*, A. Hirano, Y. Takeda, O. Yamamoto

Department of Chemistry, Faculty of Engineering, Mie University, Tsu 514-8507, Japan

HIGHLIGHTS

- The electrical conductivity of PEO₁₈LiTFSI–xPP13FSI increased with x .
- The lowest interface resistance of lithium electrode was observed in the range of $x = 1.2–1.44$.
- Lithium dendrite formation was suppressed by the addition of PP13FSI into PEO₁₈LiTFSI.

ARTICLE INFO

Article history:

Received 16 February 2012

Received in revised form

5 May 2012

Accepted 10 July 2012

Available online 17 July 2012

Keywords:

Dendrite

Ionic liquid

Lithium metal

Lithium air battery

ABSTRACT

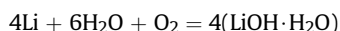
The electrical conductivity and lithium ion transport properties of the polyethylene oxide (PEO) with lithium salt Li(CF₃SO₂)₂N (LiTFSI) and a room temperature ionic liquid of *N*-methyl-*N*-propylpiperdinium bis(fluorosulfonyl)imide (PP13FSI) were examined as a function of the ionic liquid content. The electrical conductivity of PEO₁₈LiTFSI–xPP13FSI increased and the lithium ion transport number decreased with increasing the ionic liquid content. The interface resistance between PEO₁₈LiTFSI–xPP13FSI and lithium metal was dependent on x and the lowest interface resistance was observed in the range of $x = 1.2–1.44$. The critical current density of lithium deposition and dissolution on lithium metal was reduced and lithium dendrite formation was suppressed by the addition of PP13FSI into PEO₁₈LiTFSI.

© 2012 Elsevier B.V. All rights reserved.

1. Introduction

Lithium–air rechargeable batteries are considered as a promising battery system with high specific energy density due to the extremely high theoretical energy density of 11,426 W h kg^{−1} (excluding oxygen), which is comparable with that of gasoline [1]. These batteries are attracting growing attention and much R&D effort as a possible power source for electric vehicles. The system mainly consists of a lithium metal negative electrode, an electrolyte and a carbon–air positive electrode. Two types of lithium–air batteries have been developed; non-aqueous and aqueous electrolyte types. The non-aqueous system exhibits higher specific energy density than the aqueous system, but has some severe problems that must still be addressed, such as lithium metal corrosion by water, CO₂ ingress when operated in air and high polarization during the charge and discharge processes. The energy density of the aqueous system is lower than that of the non-

aqueous system by the 2371 W h kg^{−1} (excluding oxygen), because water is involved in the cell reaction as follows;



However, these problems observed in the non-aqueous system are not present or have been solved in the aqueous system. The key component of aqueous-type lithium–air batteries is the water-stable lithium-conducting solid electrolyte, since lithium metal reacts severely with water. At present, the Li_{1+x}Ti_{2–x}Al_xP₃O₁₂ (LTAP) NASICON-type solid electrolyte is the only reported water-stable lithium-conducting solid electrolyte [2]. The use of a water-stable lithium electrode for lithium–air batteries was proposed by Visco et al. [3], and Imanishi and his colleagues [4]. The water stable lithium electrode proposed by Imanishi and co-workers consisted of a lithium metal negative electrode, a PEO-based lithium-conducting polymer electrolyte of PEO–Li(CF₃SO₂)₂N (LiTFSI), and LTAP, where the polymer electrolyte is used to prevent direct contact between the lithium metal and LTAP, because LTAP is unstable in contact with lithium metal [4].

* Corresponding author. Tel.: +81 59 231 9420; fax: +81 59 231 9478.

E-mail address: imanishi@chem.mie-u.ac.jp (N. Imanishi).

The polymer electrolyte acts as a protective layer for the water-stable lithium metal electrode in aqueous lithium–air batteries and should meet requirements such as high lithium ionic conductivity, stability with lithium metal, and a low interface resistance between lithium metal and the polymer electrolyte. Kim et al. [5] reported interesting results on a composite polymer electrolyte (CPE) based on PEO and a room temperature ionic liquid of *N*-alkyl-*N*-methylpyrrolidinium bis(trifluoromethanesulfonyl)imide (PYR_{1A}TFSI). The addition of PYR_{1A}TFSI into PEO–LiTFSI resulted in a large increase of the ionic conductivity and in a decrease of the interface resistance between lithium metal and the CPE. Shin et al. [6] reported that *N*-methyl-*N*-propylpyrrolidinium TFSI (PYR13TFSI) addition into PEO inhibited the formation of crystalline polymer–salt phases and an increased fraction of amorphous region present in the CPE. Recently, Imanishi and his colleagues [7–9] have made some progress on this issue using a PEO-based polymer electrolyte with a SiO₂ nano-filler and a room temperature ionic liquid of *N*-methyl-*N*-propylpiperidinium bis(trifluoromethanesulfonyl)imide (PP13TFSI). Addition of the ionic liquid into PEO₁₈LiTFSI improved the lithium ion conductivity and reduced the interface resistance between lithium and the CPE, where ionic liquids have the same anion as that of the lithium salt in the polymer electrolyte to interact with lithium cations located in the polymer chains, which hinders the formation of crystalline phases [10].

Although a polymer electrolyte with high ionic conductivity and a low interface resistance between lithium metal and the polymer electrolyte can be achieved by the addition of room temperature ionic liquids and nano-fillers, lithium dendrite formation during the lithium deposition process is another important subject to consider for a polymer electrolyte aimed at application in lithium–air and lithium–polymer batteries. Lithium metal is the best negative electrode candidate for high energy density batteries, because it has a very high theoretical specific capacity of 3861 mA h g^{−1} and a high negative potential of −3.05 V vs. NHE. However, the formation of dendrites during lithium deposition limits the use of lithium metal as a negative electrode in lithium

batteries. This phenomenon occurs even with polymer electrolytes, although to a lesser extent than that with liquid electrolytes [11,12]. Brisson et al. [11] reported in detail on the lithium dendrite formation mechanism for Li/PEO₁₈LiTFSI/Li. Our previous results confirmed that the addition of an appropriate amount of PP13TFSI into PEO₁₈LiTFSI significantly suppressed the dendrite formation onset time [8].

In this study, the ionic conductivity and interface resistance between lithium metal and a CPE consisting of PEO₁₈LiTFSI–*x*N-methyl-*N*-propylpiperidinium bis(fluorosulfonyl)imide (PP13FSI) are examined as a function of *x*, in addition to dendrite formation during the lithium deposition process dependent on the thickness of the CPE. These properties of PEO₁₈LiTFSI–*x*PP13FSI were compared with those of PEO₁₈LiTFSI–*x*PP13TFSI. An ionic liquid with FSI anions was considered due to the fact that it exhibits lower viscosity and higher ionic conductivity than that with TFSI anions and the Li/PP13FSI–LiTFSI/LiCoO₂ cell showed better high rate charge and discharge performances than that of the Li/PP13TFSI–LiTFSI/LiCoO₂ cell [13].

2. Experimental

PEO₁₈LiTFSI–*x*PP13FSI CPEs were prepared using a casting method. PEO (Sigma–Aldrich, M_v = 600,000) was dissolved in anhydrous acetonitrile (AN) and LiTFSI (Wako Chemicals, Japan) and PP13FSI (Dai-ichi Kogyo-Seiyaku Co. Ltd., Japan) were then added to obtain an O/Li⁺ mole ratio in PEO–LiTFSI of 18. The mixed solution was stirred at room temperature for 24 h and then cast into a clean Teflon dish. The AN solvent was evaporated slowly at room temperature in an Ar-filled dry glove box. After AN was completely evaporated, the Teflon dish was transferred to a vacuum oven to dry at 100 °C for 24 h to remove the residual AN. The thicknesses of the CPEs were in the range of 100–300 μm.

The microstructure of the CPEs was observed using an optical microscope (Keyence VHX-1000) at room temperature and 60 °C. Electrical conductivity measurements of CPE were performed using

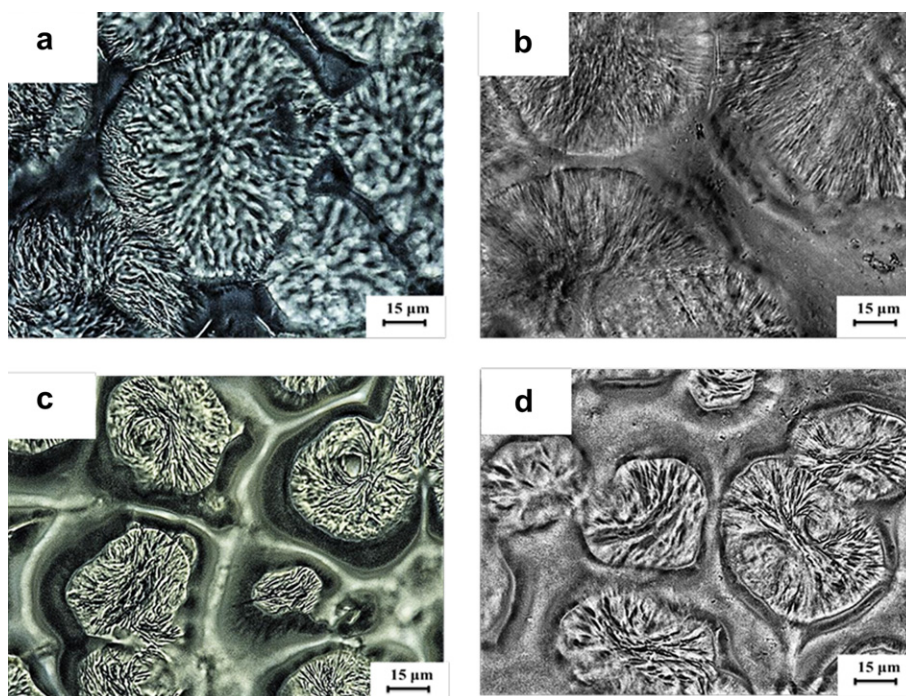


Fig. 1. Optical photographs of (a) PEO₁₈LiTFSI at room temperature, (b) PEO₁₈LiTFSI at 60 °C, (c) PEO₁₈LiTFSI–1.44PP13FSI at room temperature and (d) PEO₁₈LiTFSI–1.44PP13FSI at 60 °C.

sandwich cells of Au/CPE/Au with gold foil electrodes. The cell impedances were measured using a frequency response analyzer (Solartron 1250) in the frequency range from 0.1 Hz to 1 MHz and the temperature range 25–80 °C. Z-plot software was employed for data analysis. Li/CPE/Li sandwich cells were assembled to investigate the interface resistance between lithium and the CPE, and the electrochemical properties during lithium deposition and stripping. The active surface area was 1.00 cm². All cells were sealed into plastic film enveloped in an Ar-filled dry glove box. The plastic film envelope was then evacuated and heat-sealed. Electrochemical measurements were conducted using a multichannel Potentiostat-Galvanostat (Biologic Science Instruments VMP3). The lithium ion transport number t_{Li}^+ , was examined using a combination of AC impedance and the DC polarization method, as originally proposed by Evans et al. [14] and lately refined by Abraham et al. [15] using the Li/CPE/Li cell. The cell voltages were measured for at least 4 h to obtain steady-state current data. The diffusion coefficient was estimated using a method proposed by Ma et al. [16]. The Li/CPE/Li cell was polarized at 50 mV in potentiostatic mode for a few hours to achieve steady-state using the multichannel Potentiostat-Galvanostat, and the potential was then interrupted and monitored at 60 °C.

The thermal properties of the CPEs were examined using differential scanning calorimetric analysis (DSC; Rigaku DSC 8230) in the temperature range from –80 to 200 °C at a heating rate of 20 K min^{–1}. Lithium dendrite formation on the lithium/CPE interface was examined using a previously reported optical visualization cell [7]. The visualization images were observed using an optical microscope (Keyence VHX-1000). The distance between the two lithium electrodes was set to approximately 1 mm and the cells were sealed in the same manner as that for the sandwich cells.

3. Results and discussion

Self-supported CPE sheets of PEO₁₈LiTFSI–xPP13FSI were prepared in the range of x from 0 to 2.4, where x is the mole ratio of PP13⁺/Li⁺. The $x = 2.4$ CPE was slightly viscous and difficult to handle. Fig. 1 shows optical images of the PEO₁₈LiTFSI–1.44PP13FSI CPE at room temperature and 60 °C. Fig. 1a clearly reveals the microstructure of PEO₁₈LiTFSI at room temperature, which consists of square domains with an average size of 45 μm. Addition of PP13FSI into PEO₁₈LiTFSI results in the immersion of the ionic liquid into the gaps of the domains and connects some isolated domains into an integrated matrix, as shown in Fig. 1c. These optical images

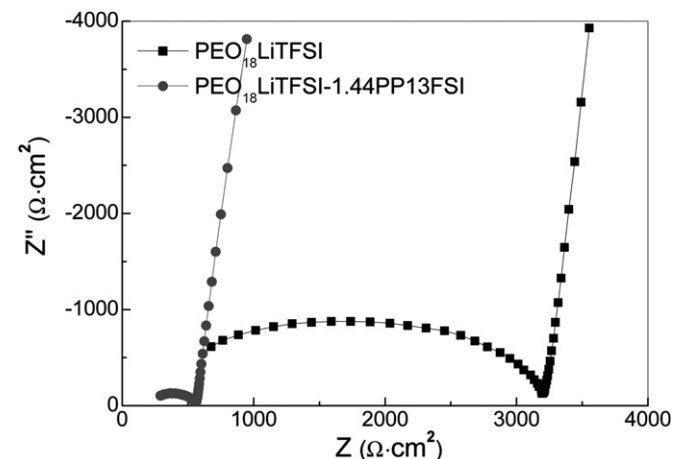


Fig. 2. Impedance profiles of (a) Au/PEO₁₈LiTFSI/Au and (b) Au/PEO₁₈LiTFSI–1.44PP13FSI/Au at 25 °C.

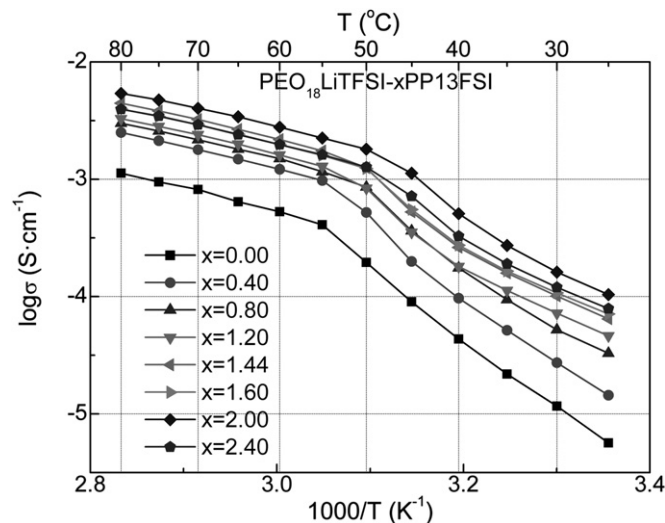


Fig. 3. Temperature dependence of the electrical conductivity for PEO₁₈LiTFSI–xPP13FSI as a function of x .

at 60 °C are similar to those at room temperature. This microstructure suggests that the ionic liquid could act as a bridge for ion transport among the PEO₁₈LiTFSI domains, which would enhance the ionic conductivity.

Fig. 2 shows an impedance profile of the Au/PEO₁₈LiTFSI–1.44PP13FSI/Au cell at room temperature with that of the Au/PEO₁₈LiTFSI/Au cell. The impedance profile of PEO₁₈LiTFSI has a large depressed semi-circle followed by a straight line. The semi-circle can be assigned as the grain boundary resistance and the intercept of the real axis at a high frequency corresponds to the bulk resistance of the polymer electrolyte. The diameter of the large semi-circle is reduced by addition of the ionic liquid into PEO₁₈LiTFSI. Thus, the grain boundary resistance of 3086 Ω cm² for PEO₁₈LiTFSI decreases to 354 Ω cm² by the addition of 1.44 mol PP13FSI. The ionic liquid in contact with the polymer grains, as shown in Fig. 1c, could reduce the grain boundary resistance among the polymer grains. On the other hand, the bulk resistance of PEO₁₈LiTFSI shows no significant change by addition of the ionic liquid. Fig. 3 shows Arrhenius plots for the electrical conductivity of PEO₁₈LiTFSI–xPP13FSI as a function of x . The conductivity increases with increasing x and a maximum conductivity of 1.04×10^{-4} S cm^{–1} at 25 °C is found for $x = 2.0$, which is almost 1 order of magnitude lower than that of PP13FSI (3.7×10^{-3} S cm^{–1} at 25 °C) [13], higher than that of PEO₁₈LiTFSI–2.0PP13TFSI (7.1×10^{-5} S cm^{–1} at 25 °C) [8], and comparable with that of PEO₁₀LiTFSI–0.96PYR₁₁SO₄TFSI (1.28×10^{-4} S cm^{–1} at 20 °C) [5]. The Arrhenius plots show

Table 1
Ionic transport properties of PEO₁₈LiTFSI–xPP13FSI.

Sample	25 °C ($\times 10^{-5}$ S cm ^{–1})		60 °C ($\times 10^{-3}$ S cm ^{–1})		E_a (kJ mol ^{–1})		t_{Li}^+	X_c (%)
	σ	σ_{Li}^+	σ	σ_{Li}^+	Low temp. region	High temp. region		
$x = 0.00$	0.56	0.13	0.53	0.13	115.7	38.8	0.24	35.9
$x = 0.40$	1.45	0.28	1.22	0.23	110.9	34.7	0.19	
$x = 0.80$	3.29	0.39	1.50	0.18	102.4	36.2	0.12	
$x = 1.20$	4.63	0.60	1.69	0.22	92.8	36.1	0.13	26.3
$x = 1.44$	6.45	0.77	2.18	0.26	92.3	36.0	0.12	26.1
$x = 1.60$	7.12	0.64	1.98	0.18	89.4	35.2	0.09	21.9
$x = 2.00$	10.4	0.83	2.78	0.22	89.9	33.8	0.08	20.6
$x = 2.40$	7.88	0.24	1.98	0.06	90.3	34.9	0.03	20.0

σ : electrical conductivity, σ_{Li}^+ : lithium ion conductivity, t_{Li}^+ : lithium ion transport number.

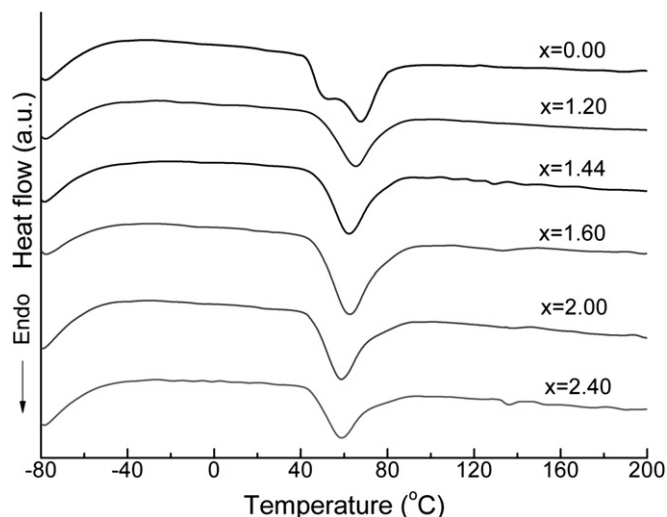


Fig. 4. DSC traces of PEO₁₈LiTFSI–xPP13FSI.

a conductivity knee at 50–60 °C, which is related to the semi-crystalline to amorphous phase transition around the melting temperature for PEO-based materials [17]. These transition temperatures decrease with increasing x in PEO₁₈LiTFSI–xPP13FSI from 55 °C for $x = 0.00$ to 47 °C for $x = 2.00$. These activation energies for ionic conduction calculated from the Arrhenius plots decrease with increasing x from 115.7 kJ mol^{−1} for $x = 0$ to 89.9 kJ mol^{−1} for $x = 2.0$ in the low temperature range and from 38.8 kJ mol^{−1} for $x = 0$ to 33.8 kJ mol^{−1} for $x = 2.0$ in the high temperature range. The conductivity data are summarized in Table 1.

In the PEO₁₈LiTFSI–xPP13FSI, the mobile ions are not only lithium ions, but also TFSI[−] and FSI[−] anions and PP13⁺ cations. The lithium ion transport number (t_{Li}^{\pm}) in the composite electrolyte is interesting for applications in electrochemical cells with a lithium electrode, because the electrode reaction is limited by the diffusion

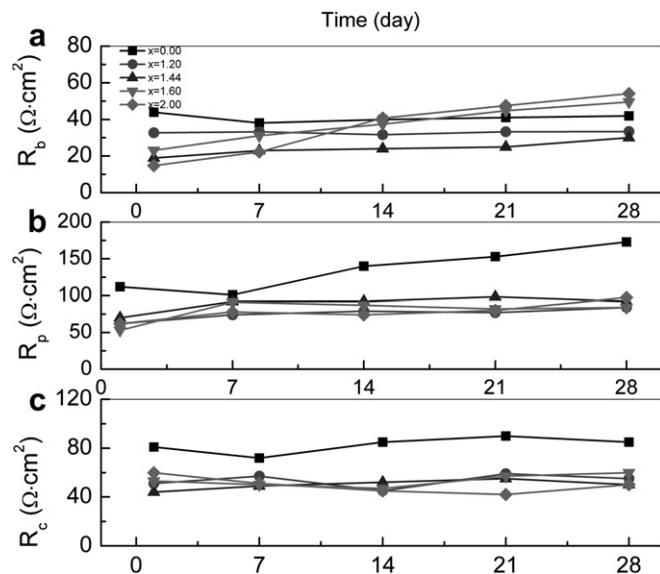


Fig. 6. Time dependence of (a) the bulk resistance, R_b , (b) passivation film resistance, R_p and (c) charge transfer resistance, R_c for the Li/PEO₁₈LiTFSI–xPP13FSI/Li cell at 60 °C.

of lithium ions in the electrolyte. Lithium ion transport number obtained by the method reported by Evans et al. [14] is summarized in Table 1. t_{Li}^{\pm} for PEO₁₈LiTFSI is comparable to that reported previously [8]. t_{Li}^{\pm} for PEO₁₈LiTFSI–xPP13FSI decreases with increasing x , from 0.24 for $x = 0.0$ to 0.08 for $x = 2.0$. The decrease of t_{Li}^{\pm} by addition of PP13FSI into PEO₁₈LiTFSI could be explained by the decrease in the mole fraction of lithium ions in the CPE. The mole fraction of Li⁺ decreases from 0.5 in PEO₁₈LiTFSI to 0.167 in PEO₁₈LiTFSI–2.0PP13FSI. Similar decrease in the lithium ion transport number was observed for PEO₂₀LiTFSI–PYR₁₃TFSI [10]. The lithium ion conductivities of PEO₁₈LiTFSI–xPP13FSI at 25 °C, as calculated from the total electrical conductivity and t_{Li}^{\pm} , are also shown in Table 1. At 25 °C, the lithium ion conductivities increase

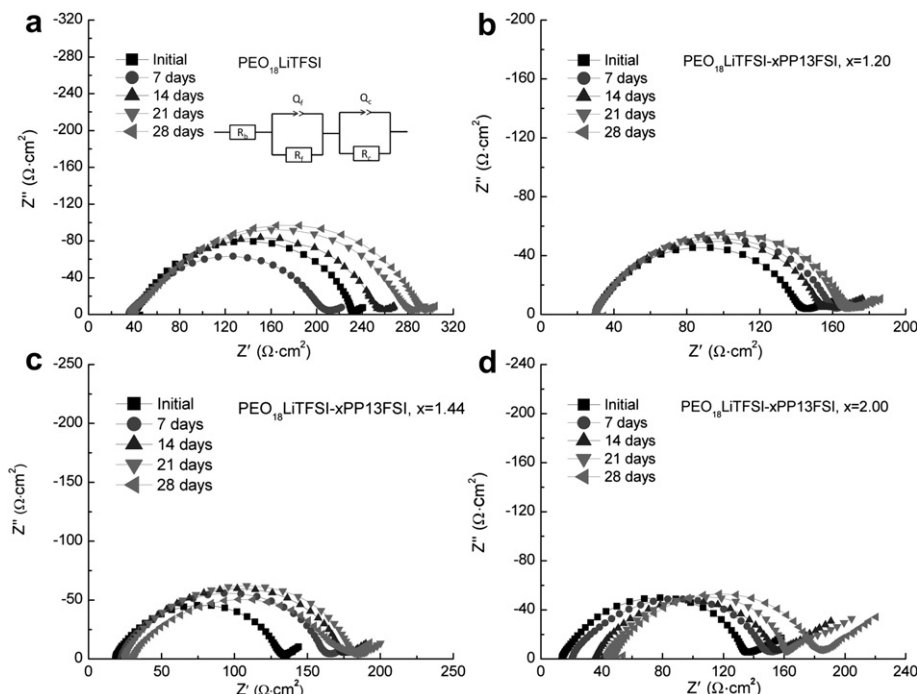


Fig. 5. Impedance spectra as a function of the storage time at 60 °C for PEO₁₈LiTFSI–xPP13FSI with $x =$ (a) 0.0, (b) 1.2, (c) 1.44 and (d) 2.00.

Table 2
Lithium ion conductivity, passivation film resistance in the sandwich cell with lithium electrode, diffusion coefficient (D), anion transport number (t_a), critical current density (J^*) and dendrite onset time (τ) of PEO₁₈LiTFSI and PEO₁₈LiTFSI–ionic liquids at 60 °C.

Polymer electrolyte	Lithium ion conductivity (S cm ⁻¹)		R_p (Ω cm ²)	D (cm ² s ⁻¹)	C_o (cm ⁻³)	t_a	L (μm)	J^* (mA cm ⁻²)		J (mA cm ⁻²)	τ (h)	
	25 °C	60 °C						Calc.	Obs.		Calc.	Obs.
PEO ₁₈ LiTFSI	1.3×10^{-6}	1.3×10^{-4}	173	3.60×10^{-8}	6.70×10^{20}	0.76	200	0.51	~0.5	0.1	15.6	140
							100	1.02	~1.0	0.3	1.7	35
PEO ₁₈ LiTFSI–1.44PP13FSI	7.7×10^{-6}	2.6×10^{-4}	92	2.25×10^{-8}	5.00×10^{20}	0.88	270	0.15	~0.2	0.1	4.05	256
							115	0.35	~0.3	0.3	0.45	68
PEO ₁₈ LiTFSI–1.44PP13TFSI	5.3×10^{-6a}	2.3×10^{-4a}	68.4 ^a	2.67×10^{-8}	6.70×10^{20a}	0.77 ^a				0.1	11.3	434 ^a
										0.25	1.80	105 ^a

t_a : anion transport number.

^a Data obtained from Ref. [8].

monotonically with increasing x up to 2.0. The anion of ionic liquids might play the role of coordinating bridges with lithium cations located in the polymer chains, which could inhibit the formation of stoichiometric EO/Li crystalline polymer-salt phases and then more fraction of amorphous region present in the CPE. The enhancement in the lithium ion conductivity may be explained by the decrease in the crystalline phase of the CPE, which was confirmed by DSC analysis.

Fig. 4 shows DSC heating traces for PEO₁₈LiTFSI–xPP13FSI. PEO₁₈LiTFSI exhibits eutectic melting. The relative fractions of the crystalline phase (X_c) in PEO₁₈LiTFSI–xPP13FSI were estimated from the heat of melting for the CPE (ΔH_m) and crystalline PEO ($\Delta H_o = 213.7 \text{ J g}^{-1}$) using the equation $\Delta H_m/\Delta H_o$, and the results are shown in Table 1. The fraction of crystalline phase decreased with increasing x . The high lithium ion conductivity of PEO₁₈LiTFSI–2.00PP13FSI with a low mole fraction of lithium ions suggests that the lithium ion mobility in the non-crystalline phase is higher than that in the crystalline phase. The low lithium ion conductivity of PEO₁₈LiTFSI–2.40PP13FSI could be explained by inaccuracy of the conductivity and ion transport number data due to the rough surface created during casting of the viscous PEO₁₈LiTFSI–2.40PP13FSI CPE. At 60 °C, where PEO₁₈LiTFSI–xPP13FSI is a molten phase, no clear dependence of x on the lithium ion conductivity was observed.

Many papers have reported that the interface between lithium metal and a polymer electrolyte has high resistance due to the formation of a passivation layer, and in many cases the interface resistance is increased with the contact period [4,18,19]. Zhang et al. [4] reported that the interface resistance between lithium metal and a PEO₁₈LiTFSI polymer electrolyte was as high as 400 Ω cm² at 60 °C after 30 days storage. Fig. 5 shows some typical impedance spectra for the Li/PEO₁₈LiTFSI–xPP13FSI/Li cell measured at 60 °C as a function of the storage period. These impedance spectra are characterized by a diminished semicircle in the high frequency region ($>10^5$ Hz) and a large slightly depressed semicircle (10^5 to 10^2 Hz) along with a straight line inclined at approximately 45°, which represents the diffusion process of ions [20]. The small semicircle in the high frequency region can be assigned to the grain boundary resistance of the CPE, and the intercept of this semicircle with the real axis can be attributed to the bulk resistance (R_b) of the CPE. The diameter of the second large semicircle is related to the overall interface resistance (R_i), which contains the resistance of the passivation film formed on the lithium metal surface (R_p) and the polymer electrolyte, and the charge-transfer resistance of the $\text{Li}^+ + e = \text{Li}$ reaction (R_c). In Fig. 6, the dependence of the bulk, passivation film and charge transfer resistances on storage time are shown as a function of x for PEO₁₈LiTFSI–xPP13FSI, where R_b and R_c are estimated from the impedance profiles using the equivalent circuit shown in Fig. 5. The bulk resistances of PEO₁₈LiTFSI and PEO₁₈LiTFSI–1.2PP13FSI show no change with the storage period,

but PEO₁₈LiTFSI–1.6PP13FSI and PEO₁₈LiTFSI–2.0PP13FSI show a significant increase of the bulk resistance with the storage period. These results suggest that PEO₁₈LiTFSI–xPP13FSI with a high content of PP13FSI is a metastable phase and the mobile Li^+ ions could be trapped by FSI⁻ ions, as reported by Huang et al. [21]. The formation of LiFSI was confirmed by DSC analysis, where a small heat flow peak due to melting of LiFSI was observed at around 130 °C, as shown in Fig. 4. The passivation film resistance between lithium metal and PEO₁₈LiTFSI was improved by the addition of PP13FSI. The initial passivation film resistance of 112 Ω cm² for Li/PEO₁₈LiTFSI/Li increased to 173 Ω cm² after 28 days, while the passivation film resistance for Li/PEO₁₈LiTFSI–1.44PP13FSI/Li increased only slightly from 70 to 92 Ω cm² after 28 days. The charge transfer resistance showed no significant change by either the addition of PP13FSI or the storage period. The cell resistance between the lithium electrode and PEO₁₈LiTFSI–xPP13FSI suggests that the best electrolyte candidate for use with a lithium metal electrode is PEO₁₈LiTFSI–1.44PP13FSI, whose passivation film resistance was slightly higher than that of Li/PEO₁₈LiTFSI–1.44PP13TFSI/Li reported in the previous paper [8]. The passivation film resistances are summarized in Table 2.

Lithium dendrite formation during the lithium deposition process is a serious problem for a high capacity lithium negative electrode. The mechanism of dendrite growth in Li/polymer electrolyte/Li has been extensively studied by Brissot et al. [11,22,23]. They reported the relation between the critical current density J^* , at which the dendrite formation is initiated and the diffusion coefficient D , as follows:

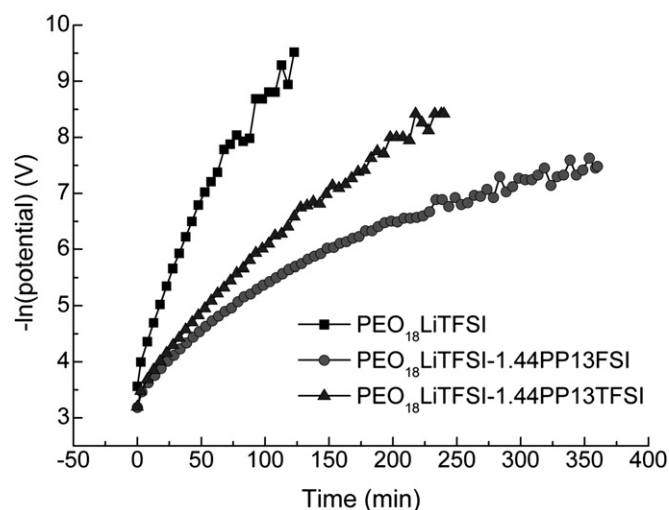


Fig. 7. Natural logarithm of potential vs. time curves for Li/PEO₁₈LiTFSI/Li and Li/PEO₁₈LiTFSI–1.44PP13FSI/Li cells at 60 °C after polarization at 50 mV.

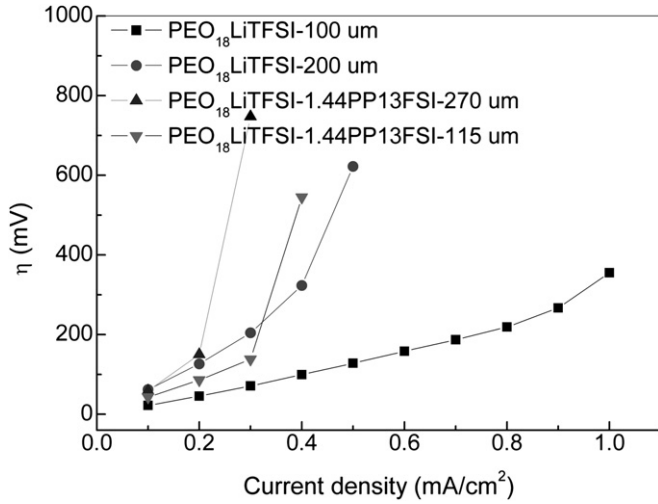


Fig. 8. Potential (η) profiles as a function of time at various current densities and at 60 °C for the Li/PEO₁₈LiTFSI/Li and Li/PEO₁₈LiTFSI–1.44PP13FSI/Li cells with different electrolyte thicknesses.

$$J^* = \frac{2eC_0D}{t_aL}, \quad (1)$$

where C_0 is the initial concentration, e is elemental charge, t_a is the anion transport number, and L is the distance between the electrodes. If L is larger than the diffusion length $l = \sqrt{D\tau}$, at time τ , then the dendrite growth onset time τ (Sand's time) [24] is given by:

$$\tau = \pi D \left(\frac{C_0 e}{2J t_a} \right)^2, \quad (2)$$

where J is the current density. The critical current density J^* , and the onset time for dendrite formation are dependent on the diffusion

coefficient of the polymer electrolyte. The diffusion coefficient was estimated using the method proposed by Ma et al. [16]. The Li/polymer electrolyte/Li cell was polarized at 50 mV for a few hours, and the potential was then interrupted and the potential decay was monitored. The diffusion coefficient is calculated from the slope of a plot of natural logarithm of potential vs. time:

$$\text{Slope} = -\frac{\pi^2 D}{L^2}, \quad (3)$$

Typical natural logarithm vs. time curves for the Li/PEO₁₈LiTFSI/Li, Li/PEO₁₈LiTFSI–1.44PP13FSI/Li and Li/PEO₁₈LiTFSI–1.44PP13FSI/Li cells at 60 °C are shown in Fig. 7. A linear relation was observed after sufficient time. The diffusion coefficients were estimated from the slopes of the linear parts. In Table 2, the calculated diffusion coefficients are summarized along with the critical current density and dendrite formation onset time calculated using these diffusion coefficients. The diffusion coefficient of PEO₁₈LiTFSI–1.44PP13FSI is comparable with that of PEO₁₈LiTFSI–1.44PP13TFSI and is slightly higher than that of PEO₂₀LiTFSI–xPYR13TFSI reported by Shin et al. [6], which was measured to be 10^{–8} cm² s^{–1} at 60 °C by the same method. The calculated critical current density of PEO₁₈LiTFSI is decreased by the addition of PP13FSI. Fig. 8 shows the change in cell potential with time at various current densities and at 60 °C for Li/PEO₁₈LiTFSI/Li and Li/PEO₁₈LiTFSI–1.44PP13FSI/Li cells with different polymer electrolyte thickness. A clear increase in cell potential is observed at a specific current density, which corresponds to the critical current density. The observed critical current densities show an inverse linear dependence on the electrolyte thickness and good agreement with the calculated values shown in Table 2. Dendrite formation and growth was observed using visualization cells with an electrode distance of approximately 1.0 mm. Fig. 9 shows typical results for Li/PEO₁₈LiTFSI/Li and Li/PEO₁₈LiTFSI–1.44PP13FSI/Li cells at 60 °C and 0.1 mA cm^{–2}. Dendrite formation is observed after 210 h and a trace dendrite was observed after 140 h for the Li/PEO₁₈LiTFSI/Li cell. These results are comparable with those we have previously

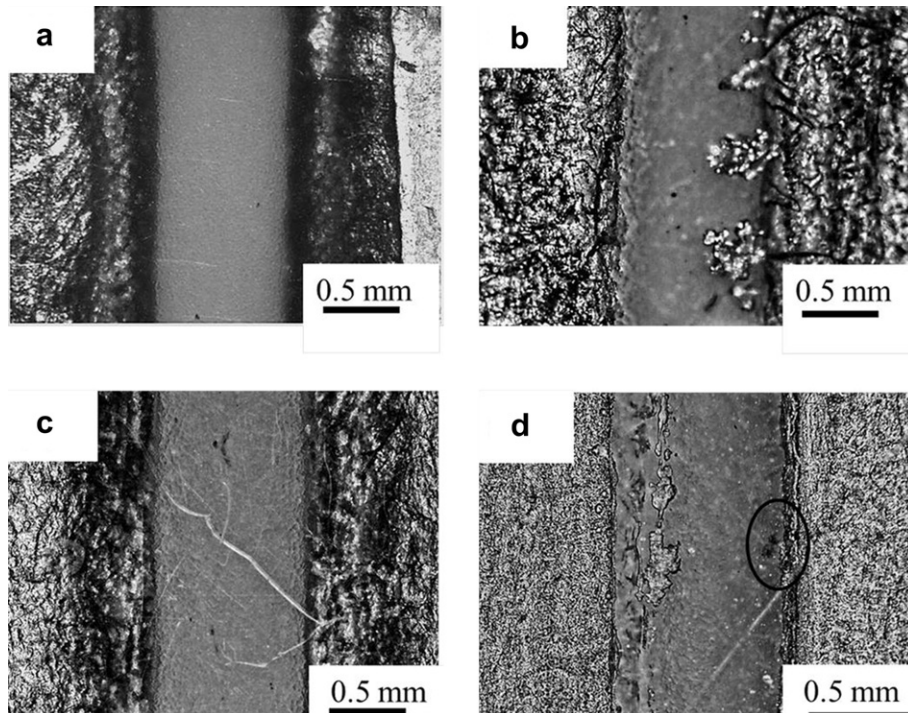


Fig. 9. Dendrite growth in the Li/PEO₁₈LiTFSI/Li and Li/PEO₁₈LiTFSI–1.44PP13FSI/Li cells at 0.1 mA cm^{–2} and at 60 °C. (a) Li/PEO₁₈LiTFSI/Li for $t = 0$ h, (b) Li/PEO₁₈LiTFSI/Li for $t = 210$ h, (c) Li/PEO₁₈LiTFSI–1.44PP13FSI/Li for $t = 0$ h, and (d) Li/PEO₁₈LiTFSI–1.44PP13FSI/Li for $t = 256$ h.

reported [7]. No clear dendrite formation was observed in the Li/PEO₁₈LiTFSI–1.44PP13FSI/Li after 256 h, but dendrite formation occurred after 334 h. The dendrite formation onset times calculated using Eq. (2) with the observed diffusion coefficients are 15.6 h for PEO₁₈LiTFSI and 4 h for PEO₁₈LiTFSI–1.44PP13FSI, as shown in Table 2, where the transport number of PP13⁺ is assumed to be very low. However, the observed onset time was increased by the addition of PP13FSI into PEO₁₈LiTFSI. Increase of the dendrite formation onset time was also observed by addition of ionic liquid PP13TFSI into PEO₁₈LiTFSI [8]. The difference between the calculated and observed dendrite formation onset times could be explained by the large diffusion length compared to the length of the examined polymer electrolyte (*ca.* 0.1 cm). The diffusion length estimated from the observed onset time of 140 h and the diffusion coefficient of $3.6 \times 10^{-8} \text{ cm}^2 \text{ s}^{-1}$ is 0.134 cm. According to Sand's theory [24], a dendrite is formed when the concentration of ions is zero at the negative electrode. When the thickness of the electrolyte is less than that of the diffusion length, the Sand's theory may not apply. In these cases, a dendrite may be formed by other factors, such as inhomogeneity of the electrode surface caused by defects and impurities on the lithium metal [11,25]. The thickness of the polymer electrolyte for application as a protective layer for a water-stable lithium electrode should be as thin as possible. The mechanism of lithium dendrite formation within the thin polymer electrolyte is now under further investigation. The composite of PEO₁₈LiTFSI with the low viscous ionic liquid PP13FSI showed higher lithium ion conductivity at room temperature and slightly higher passivation film resistance than those of the PEO₁₈LiTFSI with PP13TFSI as shown in Table 2. The observed dendrite formation onset time of the composite with PP13FSI was shorter than that of the composite with PP13TFSI, which may be due to higher passivation film resistance between lithium and PEO₁₈LiTFSI–PP13FSI than that between lithium and PEO₁₈LiTFSI–PP13TFSI [9].

4. Conclusion

The PEO₁₈LiTFSI–1.44PP13FSI CPE exhibited excellent ionic conductivity of $6.45 \times 10^{-5} \text{ S cm}^{-1}$ at 25 °C and $2.18 \times 10^{-3} \text{ S cm}^{-1}$ at 60 °C, and a low and stable interfacial resistance of approximately 142 $\Omega \text{ cm}^2$ at 60 °C in contact with lithium metal. The critical current density and lithium dendrite formation onset time were calculated using observed diffusion coefficients and compared with the experimental results. Dendrite formation was suppressed by the addition of PP13FSI into PEO₁₈LiTFSI. The observed critical current densities of PEO₁₈LiTFSI were decreased by addition of PP13FSI and were in good agreement with those calculated. The observed dendrite onset times were increased by the addition of

PP13FSI and were very far from the onset times calculated using Sand's theory. It was concluded that the dendrite formation under the present experimental conditions could not be explained by Sand's theory, and that dendrite formation may be initiated by a different reason from that proposed by Sand's theory.

Acknowledgments

This study was supported by Japan Science and Technology Agency (JST) under the project “Advanced Low Carbon Technology Research and Development Program”.

References

- [1] M. Armand, J.M. Tarascon, *Nature* 451 (2008) 652.
- [2] N. Imanishi, S. Hasegawa, T. Zhang, A. Hirano, Y. Takeda, O. Yamamoto, *J. Power Sources* 185 (2008) 1392.
- [3] S.J. Visco, N. Nimon, B. Katz, L.C.D. Jonghe, M.Y. Chu, in: The 210th Electrochemical Society Meeting, Cancun, Mexico, 2006.
- [4] T. Zhang, N. Imanishi, S. Hasegawa, A. Hirano, J. Xie, Y. Takeda, O. Yamamoto, N. Sammes, *J. Electrochem. Soc.* 155 (2008) A965.
- [5] G.T. Kim, G.B. Appetecchi, F. Alessandrini, S. Passerini, *J. Power Sources* 171 (2007) 861.
- [6] J.H. Shin, W.A. Henderson, S. Passerini, *J. Electrochem. Soc.* 152 (2005) A978.
- [7] S. Liu, N. Imanishi, T. Zhang, A. Hirano, Y. Takeda, O. Yamamoto, J. Yang, *J. Power Sources* 195 (2010) 6847.
- [8] S. Liu, N. Imanishi, T. Zhang, A. Hirano, Y. Takeda, O. Yamamoto, J. Yang, *J. Electrochem. Soc.* 157 (2010) A1092.
- [9] S. Liu, H. Wang, N. Imanishi, T. Zhang, A. Hirano, Y. Takeda, O. Yamamoto, J. Yang, *J. Power Sources* 196 (2011) 7681.
- [10] J.H. Shin, W.A. Henderson, S. Passerini, *Electrochem. Commun.* 5 (2003) 1016.
- [11] C. Brissot, M. Rosso, J.N. Chazalviel, S. Lascaud, *J. Power Sources* 81–82 (1999) 925.
- [12] T. Osaka, T. Homma, T. Momma, H. Yarimura, *J. Electroanal. Chem.* 421 (1997) 153.
- [13] H. Matsumoto, H. Sakaebe, K. Tatsumi, M. Kikuta, E. Ishiko, M. Kono, *J. Power Sources* 160 (2006) 1308.
- [14] J.H. Evans, C.A. Vincent, P.G. Bruce, *Polymer* 28 (1987) 2324.
- [15] K.M. Abraham, Z. Jiang, B. Carroll, *Chem. Mater.* 9 (1997) 1978.
- [16] Y.P. Ma, M. Doyle, T.F. Fuller, M.M. Doeff, L.C. Dejonghe, J. Newman, *J. Electrochem. Soc.* 142 (1995) 1859.
- [17] W.H. Meyer, *Adv. Mater.* 10 (1998) 439.
- [18] G.B. Appetecchi, F. Croce, G. Dautzenberg, M. Mastragostino, F. Ronci, B. Scrosati, F. Soavi, A. Zanelli, F.A. Alessandrini, P.P. Prosini, *J. Electrochem. Soc.* 145 (1998) 4126.
- [19] H.Y. Sun, H.J. Sohn, O. Yamamoto, Y. Takeda, N. Imanishi, *J. Electrochem. Soc.* 146 (1999) 1672.
- [20] R. Bouchet, S. Lascaud, M. Rosso, *J. Electrochem. Soc.* 150 (2003) A1385.
- [21] J.H. Huang, A.F. Hollenkamp, *J. Phys. Chem. C* 114 (2010) 21840.
- [22] C. Brissot, M. Rosso, J.N. Chazalviel, P. Baudry, S. Lascaud, *Electrochim. Acta* 43 (1998) 1569.
- [23] M. Rosso, C. Brissot, A. Teyssot, M. Dolle, L. Sannier, J.M. Tarascon, R. Bouchet, S. Lascaud, *Electrochim. Acta* 51 (2006) 5334.
- [24] H.J.S. Sand, *Philos. Mag.* 1 (1901) 45.
- [25] X.W. Zhang, Y. Li, S.A. Khan, P.S. Fedkiw, *J. Electrochem. Soc.* 151 (2004) A1257.